

Journal of Biomedical Optics

BiomedicalOptics.SPIEDigitalLibrary.org

Optimal optode montage on electroencephalography/functional near-infrared spectroscopy caps dedicated to study epileptic discharges

Alexis Machado
Odile Marcotte
Jean Marc Lina
Eliane Kobayashi
Christophe Grova

Optimal optode montage on electroencephalography/functional near-infrared spectroscopy caps dedicated to study epileptic discharges

Alexis Machado,^{a,*} Odile Marcotte,^{d,e} Jean Marc Lina,^c Eliane Kobayashi,^b and Christophe Grova^{a,b}

^aMcGill University, Multimodal Functional Imaging Laboratory, Biomedical Engineering Department, H3A 2B4, Québec, Canada

^bMcGill University, Montreal Neurological Institute, Department of Neurology and Neurosurgery, H3A 2B4, Québec, Canada

^cÉcole de Technologie Supérieure de l'Université du Québec, H3C 1K3, Québec, Canada

^dGERAD, École des HEC, Montréal, H3T 2A7, Québec, Canada

^eUniversité du Québec à Montréal, Département d'informatique, H3C 3P8 Québec Canada

Abstract. Functional near-infrared spectroscopy (fNIRS), acquired simultaneously with electroencephalography (EEG), allows the investigation of hemodynamic brain responses to epileptic activity. Because the presumed epileptogenic focus is patient-specific, an appropriate source/detector (SD) montage has to be reconfigured for each patient. The combination of EEG and fNIRS, however, entails several constraints on montages, and finding an optimal arrangement of optodes on the cap is an important issue. We present a method for computing an optimal SD montage on an EEG/fNIRS cap that focuses on one or several specific brain regions; the montage maximizes the spatial sensitivity. We formulate this optimization problem as a linear integer programming problem. The method was evaluated on two EEG/fNIRS caps. We simulated absorbers at different locations on a head model and generated realistic optical density maps on the scalp. We found that the maps of optimal SD montages had spatial resolution properties comparable to those of regular SD arrangements for the whole head with significantly fewer sensors than regular SD arrangements. In addition, we observed that optimal montages yielded improved spatial density of fNIRS measurements over the targeted regions together with an increase in signal-to-noise ratio. © The Authors. Published by SPIE under a Creative Commons Attribution 3.0 Unported License. Distribution or reproduction of this work in whole or in part requires full attribution of the original publication, including its DOI. [DOI: [10.1117/1.JBO.19.2.026010](https://doi.org/10.1117/1.JBO.19.2.026010)]

Keywords: functional near-infrared spectroscopy; electroencephalography; epilepsy; optical montages; optimization.

Paper 130791R received Nov. 5, 2013; revised manuscript received Jan. 13, 2014; accepted for publication Jan. 13, 2014; published online Feb. 14, 2014.

1 Introduction

Continuous wave functional near-infrared spectroscopy (CW-fNIRS) is a noninvasive imaging technique capable of measuring and mapping local changes in cerebral oxygenation caused by brain metabolic and hemodynamic activity.¹ In CW-fNIRS, a set of optic fibers, called optodes, is placed on the surface of the scalp, emitting (sources) and collecting (detectors) NIR light (16 dual sources and 32 detectors with our Brainsight CW system). Biological tissues are highly scattering but present low absorption in the NIR optical window (650 to 950 nm). Therefore, a portion of emitted photons can travel through the head up to a depth of 2 to 3 cm within the tissues following a diffusive process, reach the outermost cortex, and then be backscattered to the scalp and eventually to the detectors.² In fNIRS, the measurement channels on the scalp are defined by the different source/detector pairs (SD pairs) within a certain separation range. Indeed, the larger the separation between a source and a detector, the greater the average depth of penetration of the photons in the brain and the lower the measured diffuse reflectance signal. Based on theoretical investigations, it was demonstrated that a mean SD separation in the range of 2 to 4 cm is a good trade-off between penetration depth and signal-to-noise ratio (SNR).³

Brain activity leads to an increase in oxygen consumption, which is accompanied by an increase in cerebral blood flow

due to neurovascular coupling.⁴ This brings about changes in local oxygenated (HbO) and deoxygenated (HbR) hemoglobin concentrations and, therefore, local variations in the tissue absorption properties. HbO and HbR are two dominant NIR chromophores in cerebral tissues. Consequently, during neuronal activation periods, the variations in the amount of diffuse reflectance measured over a set of SD pairs on the scalp can be used to compute the associated changes in [HbO] and [HbR] with respect to a baseline (in what follows, [X] will denote the concentration of X and Δ will denote a variation relative to a baseline). Measurements at multiple wavelengths (e.g., 690 and 830 nm) are required to extract the concentration of each chromophore.

Either the tomographic imaging approach denoted by diffuse optical tomography (DOT)⁵ or the topographic imaging approach denoted by functional near-infrared topography (fNIRT)^{6,7} may be used in fNIRS to convert and map the variations of optical densities (Δ OD) measured on the scalp into Δ [HbO] and Δ [HbR] activity. DOT reconstructs Δ [HbO] and Δ [HbR] activity in the volume by solving an ill-posed inverse problem,^{8,9} whereas fNIRT produces topographic maps on the scalp surface using the differential modified Beer-Lambert law.^{10,11}

In fNIRS, a specific arrangement of sources and detectors on the scalp is called an SD montage and most fNIRS acquisitions are conducted using semirigid pads with the optodes arranged in a grid mesh. Early fNIRS studies were conducted with sparse, single-distance imaging arrays with the difference in locations of adjacent sources and detectors being ~ 3 cm, in order to

*Address all correspondence to: Alexis Machado, E-mail: alexis.machado@mail.mcgill.ca

obtain measurements of similar and significant cortical sensitivity. Topographic and tomographic images obtained with these sparse arrangements, however, were usually mislocalized, blurred, and distorted with respect to their original shape because of the diffuse nature of light propagation and the sparse sampling provided by the SD montages.^{12,13} It has been demonstrated using phantoms, numerical simulations, and *in vivo* experiments that the spatial resolution of images can be considerably improved using dense SD montages with overlapping measurements at multiple SD pair separations. These results have been established for fNIRS^{12,14–19} and for DOT.^{13,20–24}

Because it generally creates no interference with other imaging devices, fNIRS can be used in conjunction with other modalities, such as electroencephalography (EEG),²⁵ functional magnetic resonance imaging (fMRI),^{26,27} and magnetoencephalography (MEG).²⁸ Therefore, fNIRS has become an attractive option for the development of clinical applications that investigate neurocognitive processes associated with brain disorders.²⁹ In epilepsy research, simultaneous EEG/fNIRS offers an ideal multimodal approach for studying the relation between hemodynamic activity and spontaneous epileptic discharges detected on the scalp EEG.^{30–34} It is important to find an optimal arrangement of both the electrodes and the available sources and detectors on the scalp in order to obtain an accurate estimation of the underlying hemodynamic activity; this issue is especially important because the presumed epileptogenic focus under investigation is patient-specific and may involve different brain regions. The combination of EEG and fNIRS in the context of epilepsy, however, entails constraints on the design of SD montages.

First, in EEG/fNIRS, one does not generally use an array of optodes embedded into semirigid pads because the placing constraints on the patches conflict with the EEG montages. The pads have to be strapped on the head around the targeted region and the arrangement of the optodes has constant separations; on the other hand, the EEG electrodes must be positioned using a relative positioning system, such as the international 10/20 system or 10/10 system.^{35,36} EEG/fNIRS caps or rigid whole-head helmets allow greater flexibility in positioning optodes.³⁷ They allow EEG recordings and provide a set of possible positions (called optode holders) for holding the source or detector optodes. Contrary to what is the case in semirigid pads, the separations between the nearest and next nearest optode holders on EEG/fNIRS caps may span a large range of values and may vary by several millimeters from one subject to another because EEG/fNIRS caps are generally made of a stretchable material in order to accommodate the scalp curvature. Using EEG locations for optode holders allows for standardization of optode placement across subjects and should ensure that the brain region explored by a particular SD pair is the same across subjects taking into account the variability specific of the anatomy.³⁸ Even so, since the sensitivity of fNIRS measurements depends strongly on the thickness of the superficial tissue,³⁹ it is difficult to ensure, when using either constant or variable SD separation measurements, that a given cortical area can be measured by several SD pairs with an appropriate and homogeneous SNR level.^{12,39} With prior information on optical sensitivity, however, the differences in holder separations on an EEG/fNIRS cap may be exploited to design adequate SD montages that are subject-specific. This is the strategy we considered in this study.

Second, many studies involving multiple subjects will use the same SD montage positioned approximately at the same location in order to perform group analysis. In EEG/fNIRS

epilepsy studies, however, the epileptogenic regions to be explored with fNIRS are patient-specific.⁴⁰ Typically, the patient-specific volumes of interest (VOIs) to be explored in priority with fNIRS may result, for instance, from the segmentation of an underlying lesion in anatomical MRI,⁴¹ from the source localization of EEG^{42,43} or MEG discharges,^{44,45} and from the fMRI blood oxygen level dependent response to epileptic discharges.^{46,47} Therefore, an SD arrangement has to be designed and optimized for each individual patient. Moreover, epilepsy is organized as an underlying epileptogenic network,⁴⁸ and the simultaneous exploration of different VOIs may yield useful information. In that case, a limited number of sources and detectors must be distributed over the different VOIs.

In the present article, we describe an algorithm for computing the optimal set of positions on an EEG/fNIRS cap, where optimal means that the SD montage provides the best sensitivity to a target VOI. To do so, patient-specific light sensitivity profiles were estimated using Monte Carlo (MC) simulations and the optimization problem was formulated as a mixed linear integer programming problem.⁴⁹

2 Materials and Methods

2.1 Isometric Cap and the 10/05 EEG/fNIRS Cap

To study the hemodynamic response associated with epileptic activity, an EEG/fNIRS cap is installed on the head of the patient. The cap must fit various head shapes and offers great flexibility for SD arrangements, which is of paramount importance when designing an SD montage for a specific epilepsy patient. In this study, we propose to evaluate two possible electrode/optode holder arrangements.

The first is an isometric arrangement [Fig. 1(a)] that we have designed in collaboration with EasyCap (Germany) in order to perform EEG/fNIRS acquisitions with epilepsy patients. The cap can accommodate 63 EEG electrodes and up to 123 optodes all over the head. On this cap, both EEG electrodes [in black in Fig. 1(a)] and optode holders [in green in Fig. 1(a)] are distributed following an isometric arrangement in concentric circles. There is, on average, a distance of 3 cm between two concentric circles of optode holders; along one circle, the average distance between two holders is set to 1.5 cm. EEG circles are interleaved with the optode holder circles and do not follow a standard EEG positioning system.

Jurcak et al. have proposed to standardize optode locations on the scalp using derivatives of the international 10/20 EEG positioning system,³⁸ such as the high-density 10/05 system.⁵⁰ Therefore, the second arrangement was a 10/05 montage. EEG/fNIRS caps using a subset of this arrangement have already been proposed³⁷ [see Fig. 1(c)]. In the present article, for validation purposes, we designed a complete virtual 10/05 EEG/fNIRS cap on the skin mesh of one subject [see Fig. 1(d) and Sec. 3], following the approach proposed in Perdue et al.³⁹ The virtual 10/05 cap can accommodate 69 EEG electrodes (not shown) all over the head at the EEG 10/10 system positions and up to 248 optode holders [the black points in Fig. 1(d)] at the remaining positions of the EEG 10/05 system.

2.2 NIR Light Propagation in Biological Tissues: Monte Carlo Simulations

Given that in human tissue scattering generally dominates absorption, and assuming that any variation in light intensity

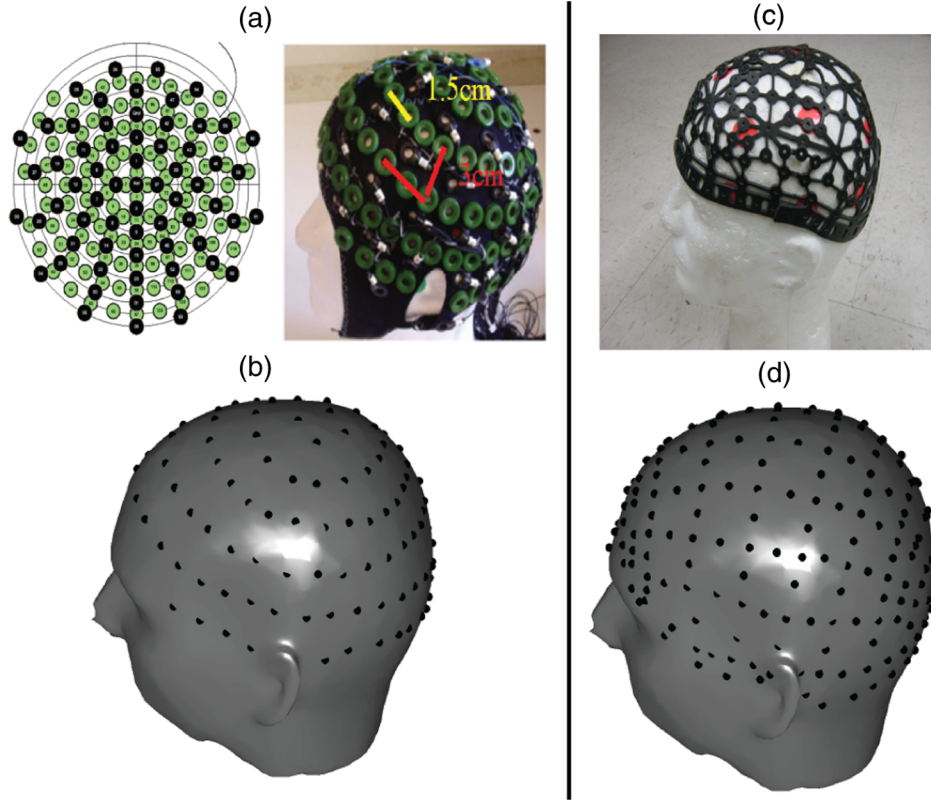


Fig. 1 (a) Electroencephalography/functional near-infrared spectroscopy (EEG/fNIRS) cap (Easy Cap, Germany) with 63 electrodes (black) and 123 optode holders (green). Left: concentric arrangement. Right: mean distance between adjacent vertical and horizontal holders. (b) Isometric arrangements of the optode holders registered on the skin surface of one subject. (c) One example of an EEG/fNIRS cap using a subset of the 10/05 arrangement. The cap has been developed by Rogue-Research (Montreal) from a collaboration with the group of S. Diamond at Dartmouth College.³⁷ (d) Virtual 10/05 arrangement of the optode holders on the skin surface of one subject.

occurs on a time-scale much greater than the mean transit time of light, the light propagation can be modeled by the time-independent diffusion equation.⁵¹

$$-D^\lambda(\mathbf{r})\nabla^2\Phi^\lambda(\mathbf{r}) + \mu_a^\lambda(\mathbf{r})\Phi^\lambda(\mathbf{r}) = S^\lambda(\mathbf{r}). \quad (1)$$

$\Phi^\lambda(\mathbf{r})$ is the photon fluence rate (W/m^2) at wavelength λ . \mathbf{r} is the position vector in the volume space V . $D^\lambda(\mathbf{r}) = 1/3\mu_s^\lambda(\mathbf{r})$ is the photon diffusion coefficient with $\mu_s^\lambda(\mathbf{r})$ the reduced scattering coefficient (mm^{-1}), which is the reciprocal of the photon random walk step length. $\mu_a^\lambda(\mathbf{r})$ is the absorption coefficient (mm^{-1}). $S^\lambda(\mathbf{r})$ is the source distribution of photons (W/m^3).

During brain activity, regional changes in blood flow and volume alter the concentration of hemoglobin in the brain and, therefore, change the absorption of the tissue.

$$\mu_a^\lambda(\mathbf{r}) = \mu_{a,o}^\lambda(\mathbf{r}) + \Delta\mu_a^\lambda(\mathbf{r}). \quad (2)$$

$\mu_{a,o}^\lambda(\mathbf{r})$ denotes the baseline absorption. If we consider an optical measurement between a source i and detector j positioned at \mathbf{r}_i and \mathbf{r}_j , the solution $\Phi^\lambda(\mathbf{r}_j, \mathbf{r}_i)$ of the photon diffusion equation after the perturbation is obtained using the Rytov approximation.⁵¹

$$\Phi^\lambda(\mathbf{r}_j, \mathbf{r}_i) = \Phi_o^\lambda(\mathbf{r}_j, \mathbf{r}_i) \exp[\psi^\lambda(\mathbf{r}_j, \mathbf{r}_i)], \quad \text{with} \quad (3)$$

$$\psi^\lambda(\mathbf{r}_j, \mathbf{r}_i) = \int_V \frac{1}{D^\lambda(\mathbf{r})} G^\lambda(\mathbf{r}, \mathbf{r}_j) \Phi_o^\lambda(\mathbf{r}, \mathbf{r}_i) \Delta\mu_a^\lambda(\mathbf{r}) d\mathbf{r}. \quad (4)$$

$\Phi_o^\lambda(\mathbf{r}, \mathbf{r}_i)$ is the fluence distribution at the baseline state (before the perturbation). $G^\lambda(\mathbf{r}, \mathbf{r}_j)$ is the Green's function of the diffusion equation at the baseline state. The Green's function is the solution of Eq. (1) considering an infinitely small point source (represented analytically as a Dirac delta function in space) at position \mathbf{r}_j . The ratio of light that reaches the detector after a variation in the underlying tissue absorption is reported as a change in optical density ($\Delta\text{OD}_{i,j}^\lambda$) and defined as

$$\Delta\text{OD}_{i,j}^\lambda = -\log_e[\Phi^\lambda(\mathbf{r}_j, \mathbf{r}_i)/\Phi_o^\lambda(\mathbf{r}_j, \mathbf{r}_i)] = \psi^\lambda(\mathbf{r}_j, \mathbf{r}_i). \quad (5)$$

Using Eq. (5) in a discrete volume (N voxels), the optical density can be rewritten as follows:

$$\Delta\text{OD}_{i,j}^\lambda = \sum_{v=1}^N \frac{1}{D^\lambda(\mathbf{r}_v)} G^\lambda(\mathbf{r}_v, \mathbf{r}_v) \Phi_o^\lambda(\mathbf{r}_v, \mathbf{r}_v) \Delta\mu_a^\lambda(\mathbf{r}_v) \delta V, \quad (6)$$

where v is the voxel index, \mathbf{r}_v is the voxel center position, δV is the volume of a voxel, and $\mathbf{r}_v, \mathbf{r}_v$ are the source and detector positions. Considering the set of SD measurements, Eq. (6) can be rewritten using the following matrix product:

$$\Delta\mathbf{OD}^\lambda = \mathbf{A}^\lambda \Delta\boldsymbol{\mu}_a^\lambda. \quad (7)$$

$\Delta\mathbf{OD}^\lambda$ is a column vector describing the change in OD for each measurement (i, j) , $\Delta\boldsymbol{\mu}_a^\lambda$ is a column vector describing the change in absorption for each voxel in the volume, and \mathbf{A}^λ is a matrix (number of measurements by number of voxels) whose each row is a vector \mathbf{a}_{ij}^λ containing the scalar sensitivity coefficients $a_{ij}^\lambda(v)$ (mm) of a particular SD measurement (i, j) to changes in absorptions within each voxel v . In \mathbf{A}^λ , the solutions $\Phi_o^\lambda(\mathbf{r}_v, \mathbf{r}_{v_i})$ and $G^\lambda(\mathbf{r}_v, \mathbf{r}_{v_j})$ can be computed using analytical or numerical methods of light propagation in biological tissues.⁸ For realistic optical montages and complex head geometries, the numerical solutions methods, such as finite element or MC simulation, are mandatory.^{51,52} Indeed, the sensitivity profile depends on the local individual anatomy.^{3,53,54}

In this study, the solution $G^\lambda(\mathbf{r}_v, \mathbf{r}_{v_h})$ associated with each optode holder h has been obtained through an MC approach,⁵² which can take into account the specific anatomy of each patient using a realistic multilayered head model built from the anatomical magnetic resonance imaging (MRI) of the subject. The MC method simulates photon transport in tissues. A photon packet with a specific weight is launched into the medium from a source point consisting of the accurate position of one of the optode holders coregistered to the anatomical MRI. The interaction of the photon packet with matter is treated as a stochastic process, where each randomly selected interaction causes a random change in the direction of the path of the photon packet propagation as well as in its weight, until it is either terminated or reflected. Any number of photon packets can be launched and modeled, until the resulting solution has the desired statistical SNR. The MC method is equivalent to the modeling of photon transport analytically by the radiative transfer equation, and it provides accurate solutions especially in the cerebrospinal fluid (CSF) (where the diffusion approximation may not hold). To decrease the computational burden, we used the MC method implemented in the Monte Carlo eXtreme software by Fang and Boas.⁵⁵ This implementation uses massively parallel computing techniques, thanks to graphics processing units (2 Nvidia Tesla cards), and is extremely fast ($\times 300$) when compared with traditional single-threaded CPU-based simulations.

2.3 Optimization of the SD Montage over the VOIs

The goal of the present study is to propose a method for finding the discrete positions of sources and detectors among the set of possible optode holder positions on an EEG/fNIRS cap. The choice of the discrete positions should maximize the spatial sensitivity profile of $\Delta\mathbf{OD}$ measurements in the target VOIs.

We formulated the problem as a mixed integer linear programming problem. Let n (resp. m) denote the number of sources (resp. detectors) to be installed and $H = \{1, 2, \dots, l\}$ the set of holder position indices. The variable x_p (for $p \in H$) is a binary variable that equals 1 if and only if a source is placed in the holder p . Similarly, y_q (for $q \in H$) is a binary variable that equals 1 if and only if a detector is placed in the holder q . For an SD measurement between holders p and q , V_{pq} denotes the sum of the sensitivity coefficients over the voxels (v) in given VOIs.

$$V_{pq} = \sum_{v \in \text{VOIs}} a_{i,j}(v), \quad (8)$$

with source i positioned at holder p and detector j positioned at holder q . For each possible combination of optode holders on the

cap (one holder is considered as a source and the other as a detector), the row vector \mathbf{a}_{ij}^λ of sensitivity coefficients was computed using the Green's solutions provided by the MC simulations and Eq. (6). In our study, we generated an optimal montage for both wavelengths, and V_{pq} was defined by using for each voxel the average of the $a_{i,j}^{830 \text{ nm}}(v)$ and $a_{i,j}^{690 \text{ nm}}(v)$ coefficients, which have similar orders of magnitude. Finally, we define

$$w_q^V = \delta(y_q - 1) \sum_{p \in H} V_{pq} x_p, \quad (9)$$

with δ denoting the delta Dirac function. The expression w_q^V represents the total contribution to sensitivity of all pairs formed by a detector positioned at holder q and any source. Considering that the components of the vectors \mathbf{x} and \mathbf{y} are x_p and y_q (respectively), the optimization problem can be formulated as follows:

$$(\hat{\mathbf{x}}, \hat{\mathbf{y}}) = \operatorname{argmax}_{\mathbf{x}, \mathbf{y}} \left(\sum_{q \in H} w_q^V \right), \quad (10)$$

with the following three sets of constraints:

1. Any source or detector is positioned at exactly one optode holder, that is,

$$\sum_{p \in H} x_p = n, \quad \sum_{q \in H} y_q = m, \quad (11)$$

2. The definition of w_q^V can be implemented by the following constraints:

$$0 \leq w_q^V \leq M y_q \quad \forall q \in H, \quad (12)$$

$$w_q^V \leq \sum_{p \in H} V_{pq} x_p \quad \forall q \in H, \quad (13)$$

where M is a large constant, greater than any of the V_{pq} . The first of these constraints implies that $w_q^V = 0$ holds whenever $y_q = 0$. Note that in any optimal solution of the model, w_q^V will actually equal $\min(My_q, \sum_{p \in H} V_{pq} x_p)$ since the objective function is the sum of the w_q^V and must be maximized.

3. A source and a detector cannot be positioned at the same holder, that is,

$$x_p + y_p \leq 1 \quad \forall p \in H. \quad (14)$$

This mixed integer linear programming problem was solved using a branch-and-bound algorithm; we refer the reader to Land and Doig⁴⁹ and to the book by Nemhauser and Wolsey.⁵⁶ In this case, the branch-and-bound algorithm consists of solving the linear relaxation of the above model, i.e., replacing the constraints that x_p and y_q are binary variables by the constraints that x_p and y_q are nonnegative real variables. Then the problem can be solved by the simplex algorithm for linear programming (see, for instance, Ref. 57). If the solution of the linear program includes a fractional variable (for instance, if x_p equals 0.5 for some p), one creates two subproblems: one in which x_p equals 0 and one in which x_p equals 1. If both of these subproblems have integer solutions, they are compared and the best one is an optimal solution of the original problem.

Otherwise new subproblems are created. The reader will find in the references quoted above a description of the whole procedure, including techniques for accelerating the branch-and-bound procedure. Algorithms for linear and integer linear programming have been implemented in several software. We have solved our model using MATLAB® (MathWorks, Massachusetts), which includes the ILOG CPLEX MATLAB® toolbox (IBM, version 13, <http://www-01.ibm.com/software/commerce/optimization/cplex-optimizer/>).

3 Validation

3.1 Isometric and 10/05 Arrangements on the Anatomical Head Model

In order to initialize the optical properties required for MC simulations, an anatomical head model was built from the classification into five tissue types [scalp, skull, CSF, gray matter (GM), and white matter (WM)] of the T1-MRI-scan of a human subject, previously acquired under an fMRI/fNIRS protocol approved by the ethics committee of the Montreal Neurological Institute and the McConnell Brain Imaging Center. The T1-MRI was obtained on a Siemens MAGNETOM 3T MRI scanner [repetition time (TR) = 2.3 s, echo time (TE) = 2.98 ms, flip angle = 9 deg]. The MRI volume was contained within an array of (192,256,256) voxels with a resolution volume of 1 mm³. The classification approach^{58–60} combines an iterative, hierarchical, nonlinear registration procedure and a three-dimensional (3-D) digital model of human brain anatomy containing both volumetric intensity-based data and a geometric atlas.⁶¹ A slice from the classified head volume is shown in Fig. 2(a).

Based on estimates available from the literature,⁶² absorption and scattering coefficient values at 830 and 690 nm were associated with each tissue type constituting the segmented anatomical head model (Table 1). The anisotropy coefficient of tissues was set to 0.9 and the refractive indices of air and tissue were assumed to be 1.0 and 1.37, respectively.

After an appropriate placement of the isometric EEG/fNIRS cap on the subject head, the 123 holder positions were digitized using the Brainsight 3-D localizer device and coregistered to the anatomical MRI of the subject using a rigid body transformation⁶³ based on anatomical landmarks (tip of the nose, nasion, left and right preauricular points). A mesh of the subject skin (86,111 vertices, mean distance between vertices: 1.4 mm ± 0.4 mm) was also obtained from the T1-MRI using the Brainstorm software.⁶⁴ The 123 holder positions were projected on the skin mesh [Fig. 1(b)]. Considering only SD pairs with interoptode separations between 1 and 5 cm, this isometric optode holder arrangement allowed for 732 possible SD measurements.

In order to test the performance of the 10/05 arrangement, we also designed a virtual 10/05 arrangement with 317 positions on the same skin mesh, following the approach proposed by Perdue et al.³⁹ Four landmarks (nasion,inion, and left and right preauricular points) were manually identified on the skin mesh. Then the NFRI MATLAB® toolbox³⁸ was used to find the 10/10 positions on the head model. A linear transformation matrix was calculated from the 10/10 coordinate locations in Montréal

Table 1 Absorption/scattering (mm⁻¹) coefficients used for the Monte Carlo simulations.

Tissues	690 nm	830 nm
Scalp	0.0159/10	0.0191/8.25
Skull	0.0101/12.5	0.0136/10.75
Cerebrospinal fluid	0.0004/0.125	0.0026/0.125
Gray matter	0.0178/15.625	0.0186/13.875
White matter	0.0178/15.625	0.0186/13.875

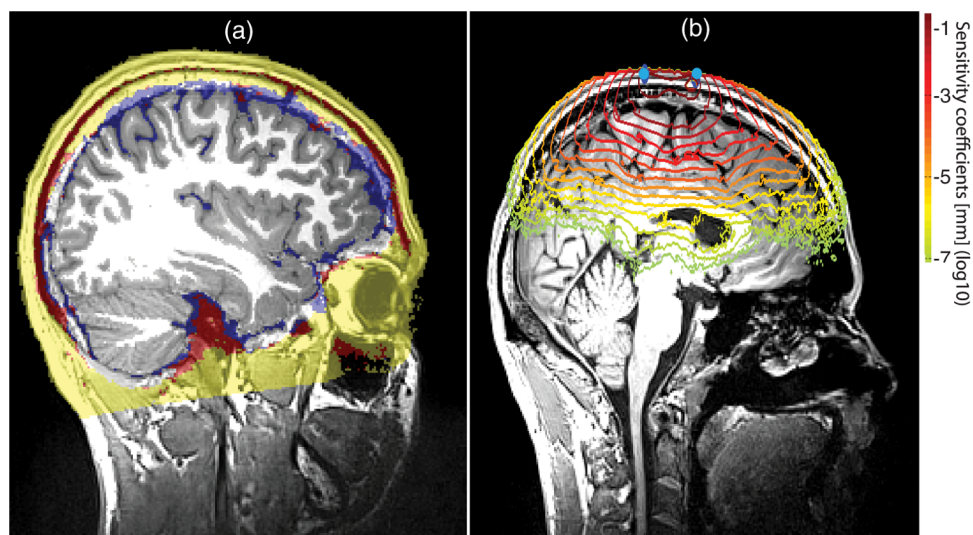


Fig. 2 (a) Classification of the anatomical magnetic resonance imaging (MRI) into five layers. Each tissue is coded with the following color label: yellow=skin; red=skull; blue=cerebrospinal fluid; gray=gray matter; white=white matter. (b) Sensitivity matrix coefficients of one source/detector (SD) pair. The optode positions are displayed in blue. For visualization purpose, a log base 10 transformation was applied to the coefficients. One contour line is shown for each order of magnitude change.

Neurological Institute (MNI) space⁵⁰ to the 10/10 coordinates on the scalp of the segmented head model. This transform was applied to the MNI 10/05 coordinate locations⁵⁰ to find the remaining 10/05 locations on the model. For this study, the 10/10 positions (69 points) were reserved for EEG electrodes, whereas the remaining 248 positions were defined as potential candidates for fNIRS optodes [Fig. 1(d)]. Keeping only pairs with interoptode separations between 1 and 5 cm, this configuration allowed for a total of 2645 possible SD measurements.

3.2 Computation of Sensitivity Coefficients

Green's functions $G^\lambda(\mathbf{r}_v, \mathbf{r}_{v_h})$ of each optode holder (located at voxel v_h) of the isometric and 10/05 arrangements were estimated by MC simulations. For each simulation, 100 million photons with a unit survival weight were launched in order to provide results with low statistical noise. Eight (resp. 16) hours were necessary to compute the Green's functions at 830 and 690 nm for all the holder positions of the isometric (resp. the 10/05) arrangement. The sensitivity profiles $\mathbf{a}_{i,j}^\lambda$ of each of the 732 (resp. 2645) possible pairs of optode holders on the isometric (resp. 10/05) arrangement were calculated using Eq. (6). A slice of one sensitivity profile at 830 nm for a particular SD measurement is shown in Fig. 2(b) and overlaid on the anatomical MRI of the subject.

3.3 Simulation of Regional Brain Activity in the Cortex

To verify that the proposed optimization method actually finds an adequate montage, we simulated 20 configurations with one focal (20 mm diameter) spherical VOI at different locations in the left hemisphere of the anatomical head model. In epilepsy research, it is often necessary to compare brain activity from the presumed focus with its corresponding homologous contralateral brain area, assumed to be normal. This is the reason why we simulated VOIs in the left hemisphere only. In such a configuration, fNIRS data acquisition will consist of mirroring the montage obtained on one side. The VOI centroids were positioned randomly in the GM with a minimal separation constraint of 10 mm between them and a maximal distance from the skin layer of 25 mm. The volume of each VOI was constrained within the GM and each voxel lying outside the GM was removed. We also simulated 20 configurations with one extended spherical VOI (50 mm diameter). The same centroids were used. Figures 3(a) and 3(b) illustrate examples of one focal versus one extended VOI.

To evaluate how the optimal positioning algorithm behaves when multiple VOIs need to be targeted simultaneously, we also simulated 20 configurations composed of two focal VOIs (with a minimum separation of 5 cm). Finally, we simulated 20 configurations involving two mirrored VOIs (i.e., a total of four VOIs). These configurations were proposed to mimic situations in which we plan to use fNIRS to target two different brain regions with their corresponding contralateral regions. We will refer to these last two configurations as the double VOIs and symmetrical VOIs configurations. Figures 3(c) and 3(d) illustrate, respectively, a double and a symmetrical configuration.

In each simulated VOI, we assumed homogeneous changes in absorption of $\Delta\mu_a^{830} = 0.0005 \text{ mm}^{-1}$ and $\Delta\mu_a^{690} = -0.0002 \text{ mm}^{-1}$, mimicking [HbO] and [HbR] changes of $\sim 5\%$ from their baseline concentration; this is a realistic estimation of the variation usually encountered during functional activations.

For any montage, the change in optical density at 830 and 690 nm can be calculated using Eq. (7) for each SD pair.

3.4 Parameters of the Optimization Model

Among all the 16 dual-wavelength sources and 32 detectors available with the Brainsight fNIRS system, we used half the optodes available, which would allow us to mirror the final montage to acquire homologous contralateral regions as well. Therefore, the configuration parameters of the optimization model are $n = 8$ sources and $m = 16$ detectors among a choice of $l = 123$ optode holders when performing the optimization on the EEG/fNIRS cap with the isometric arrangement [Fig. 1(b)] and $l = 248$ optode holders when performing the optimization on the virtual 10/05 arrangement [Fig. 1(d)]. In the simulation configuration involving two symmetrical VOIs, we used all the optodes available on the system, i.e., in this case, $n = 16$ sources and $m = 32$ detectors. The branch-and-bound algorithm was launched for each of the simulated VOI configurations and each optode holder arrangement separately.

3.5 Comparison of the Optimal Montages with Regular Arrangements of Sources and Detectors

Once the isometric optimal (O_I) and 10/05 optimal ($O_{10/05}$) montages were obtained for each simulated VOI, ΔOD^{830} and ΔOD^{690} were calculated for each SD pair of the montage. Then the topography was estimated by mapping the resulting value at each channel location (or sampling point). A channel location was defined as the middle point between the corresponding source and detector. The topography was then interpolated on the skin mesh using an inverse distance weighting interpolation scheme as in Aihara et al.⁶⁵ and Takeuchi et al.⁶⁶ The topographic maps were finally compared with the maps obtained when using three other arrangements of sources and detectors that we will consider as references.

1. Double density (DD) montages are often considered to provide an optimal contrast-to-noise ratio in activation imaging.^{12,14-19} Therefore, we compared our O_I and $O_{10/05}$ montages with a virtual DD montage composed of 8 sources and 11 detectors (24 pairs). The optodes were interleaved in a specific pattern as shown in Fig. 4(a). For each VOI, the DD montage was positioned automatically over the volume to illuminate. To do so, the centroid of the simulated VOI was first orthogonally projected on the skin surface. We then designed a two-dimensional (2-D) planar DD montage centered on this point and oriented tangentially to the skin surface. The optode positions of this 2-D montage were finally projected on the skin surface. For all VOIs, the resulting DD grids were regular with a mean distance of 15 mm (± 1 mm) between neighboring optodes. For all DD montages, MC simulations were performed to calculate the corresponding sensitivity matrices. Because a DD montage has a limited spatial coverage of the head, no DD montages were created for the double and symmetrical configurations.
2. With the isometric EEG/fNIRS cap, a simple configuration is to arrange sources and detectors in alternating

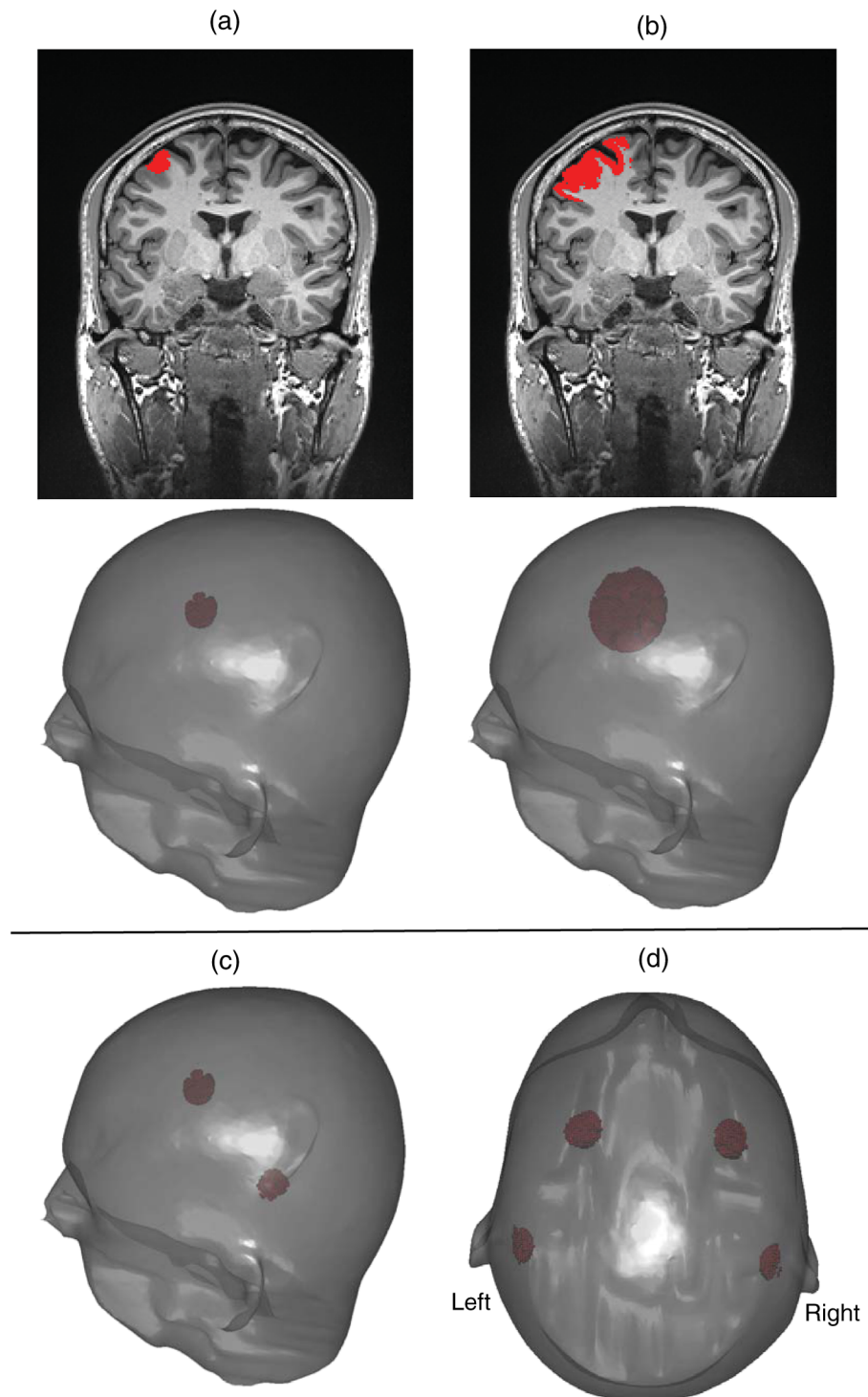


Fig. 3 (a) Representation of a single focal volume of interest (VOI). (b) Representation of a single extended VOI. The top row represents an axial slice of the anatomical MRI with the corresponding simulated VOIs (red), whereas the bottom row shows a three-dimensional (3-D) representation of the VOIs (red) and the skin mesh. (c) 3-D representation of a double VOI. (d) 3-D representation of a symmetrical VOI.

circles at optode holder locations. Therefore, we designed a virtual whole-head regular isometric (R_I) montage on the EEG/fNIRS cap with 60 sources and 63 detectors (466 pairs) as illustrated in Fig. 4(b). Because we had already calculated the sensitivity profiles of each possible pair on the isometric EEG/fNIRS cap, no additional MC simulations were required.

Obviously, such a whole-head configuration is not feasible experimentally with the typical number of sources and detectors currently available with fNIRS systems.

3. A virtual whole-head configuration following the 10/05 system with sources and detectors arranged in

alternating coronal rows has been proposed by Perdue et al.,³⁹ who demonstrated that this arrangement provides a relatively uniform sensitivity across the cortex. Using the available 248 optode positions of the virtual 10/05 cap, we designed a whole-head regular 10/05 ($R_{10/05}$) montage with 92 sources and 156 detectors (1250 pairs) arranged in alternating coronal rows [Fig. 4(c)]. Because we had already calculated the sensitivity profiles of every possible pair on the virtual 10/05 EEG/fNIRS cap, no additional MC simulations were required. Again, such a whole-head configuration is not feasible experimentally but will be used for comparison.

3.6 Validation Metrics

For each simulation configuration, a binary ground truth (GT) map on the skin was first defined as follows: we first identified the vertex of the skin surface with minimal distance to the center of mass of the VOI. All other voxels of the VOI were then projected to the skin surface following a normal to the tangential plane at this location. Let Q denote the number of active vertices (value = 1) in this map denoted by \mathbf{T}_{GT} . In the same way, let \mathbf{T}_{O_1} , \mathbf{T}_{R_1} , $\mathbf{T}_{O_{1005}}$, $\mathbf{T}_{R_{1005}}$, and \mathbf{T}_{DD} denote the topographies of the optimal isometric, regular isometric, optimal 10/05, regular 10/05, and DD montages. The skin vertices set was then divided in two regions. As shown in Figs. 5(a) and 5(b), the first region illustrated in red was the projected VOI that we considered as the GT. The second region illustrated in green, called region of background, was defined as all connected vertices along the skin surface in the neighborhood of the GT up to an order of 15 connections along the mesh. P will denote the number of vertices in the region of background.

To quantify the performances of the optimal montages when compared to the DD and whole-head regular montages for each VOI configuration, we propose three validation metrics. Validation metrics were evaluated using topographic maps obtained at 690 and 830 nm.

1. Detection accuracy: We propose a criterion based on receiver operating characteristic (ROC) curves⁶⁷ following the approach suggested by Grova et al.⁶⁸ Let
2. Sensitivity: To assess the ability of the optimal montage to map the volumetric absorption changes into OD

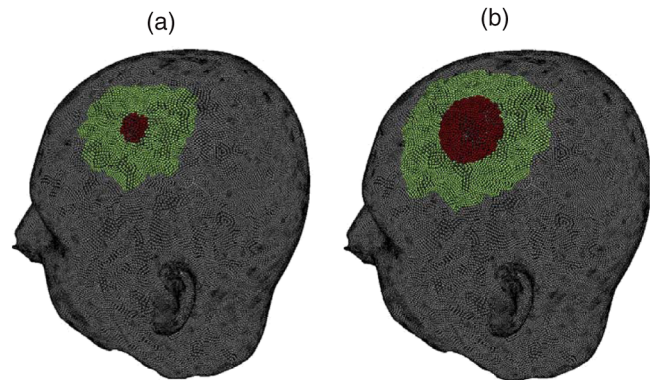


Fig. 5 Representation of the vertices belonging to ground truth (GT) (red) and the region of background (green) area for one focal (a) and one extended VOI (b).

\mathbf{T} denote the ΔOD topography of one of the five montages under investigation at one wavelength. For a threshold β chosen in the interval $[0,1]$, we considered the k 'th vertices of \mathbf{T} as active if its normalized energy is $> \beta$. Using the \mathbf{T}_{GT} as a reference, we were able to quantify the sensitivity and specificity for each threshold β and then draw the ROC curves. The area under the ROC curve (AUC) was used as detection accuracy index. It quantifies the detection ability in a close neighborhood of the GT, assessing whether the activity and its spatial extent were accurately recovered or not. Any overestimation or underestimation of the spatial extent of the GT should then affect this criterion. To interpret the AUC as a detection accuracy index, one should provide the same number of active and inactive vertices to the ROC analysis. Therefore, to calculate the amount of false positives and true negatives, we drew randomly Q vertices within the region of background. We performed this estimation randomly 20 times in order to average the AUC scores and get robust statistics (for further details see Grova et al.⁶⁸).

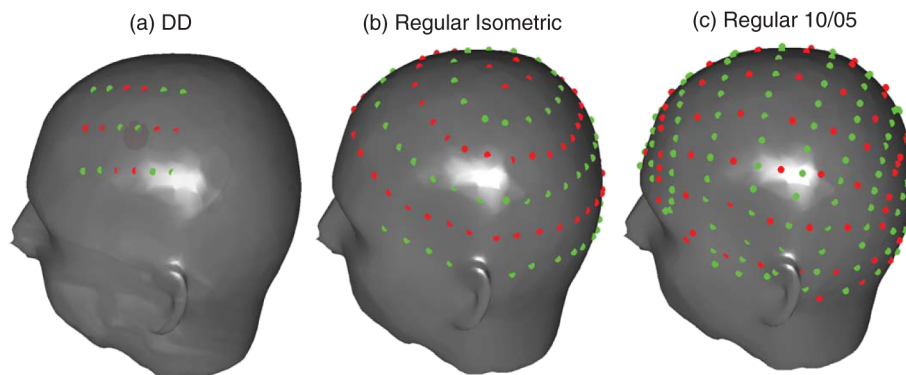


Fig. 4 Reference montages. Sources appear in red and detectors in green. (a) Double density (DD) SD montage. (b) Regular isometric SD montage. Note that on the cap used to design this montage, 63 EEG electrodes (not shown) are positioned in concentric circles between the sources and the detectors. (c) Regular 10/05 SD montage. Note that the 10/10 positions (along the vertical lines of the sources) were left blank with no optode in order to allow the installation of a 10/10 EEG montage.

signals with maximum amplitude, an absolute local energy criterion (LE) was computed as follows:

$$LE = \sum_{u=1}^Q T(u)^2. \quad (15)$$

u is the vertex index on the GT.

3. Optimal sensing: To assess the amount of measurements overlap in each voxel, an overlap map was generated by thresholding and binarizing each row of the sensitivity matrix \mathbf{A} at 2% of its maximum value (as suggested in Tian et al.¹³). The number of overlapping measurements at each voxel was counted as the sum of contributions from all SD pairs for a given montage. The 2% threshold was chosen empirically after some tests have been performed in order to provide measurement density maps that have nonzeros coefficients within the cortical aspects of the GM volume. From this overlap map, we calculated the ratio of visible voxels (overlap score >1) within the VOI and the mean value of the overlap score among the visible voxels.

4 Results

The process of optimization was fast; for one montage the convergence of the branch-and-bound algorithm was reached in only few seconds on a processor IntelCore2 Quad CPU Q940.

For each montage type and VOI configuration (single focal, single extended, double, and symmetrical), Figs. 6 and 7 show the ΔOD topographic maps generated by an absorption change in one simulated VOI. The corresponding sources (blue) and detectors (green) for each montage are shown on the scalp surface. The maps, represented using a yellow-to-red linear color scale, were normalized by their maximum value and the black isolines in each map indicate the half-maximum ΔOD values. In this section, we present only results obtained at 830 nm since results at 690 nm were very similar.

For the simple focal VOI (Fig. 6, left), the maps of all montages are well localized with the maximum ΔOD value lying in the GT area [Fig. 6(a)]. A statistical analysis performed on the 20 VOIs revealed that the mean Euclidean distance between the center of gravity of the GT maps and the estimated maps was <5 mm for all montages. The topographic map associated with the DD montage [Fig. 6(b)] was the closest to the GT map. This could be expected since the DD montage was optimized to be exactly centered on the target VOI, whereas all other montages were optimized on the fixed optode holder positions. The O_I and R_I maps [Figs. 6(c) and 6(d)] were more extended than the GT area and slightly distorted. In this particular case, it is interesting to notice that the optimal positioning algorithm found positions for the eight sources, at exact positions of the regular isometric montage. This result has been observed for 3 out of 20 simulated VOIs. The $O_{10/05}$ and $R_{10/05}$ maps [Figs. 6(e) and 6(f)] appeared less blurred than the isometric montages likely due to the denser spatial sampling. The optimal positioning algorithm attributed five out of eight sources near the GT area. Three sources were positioned in the periphery and only provide weak ΔOD amplitude.

For the extended VOI (Fig. 6, right), the DD map was again the closest to the GT map. O_I and R_I maps provided more

spatially extended topographies than the GT. The optimal positioning algorithm found almost the same source positions for the focal versus the extended target VOI except for one source, which was moved to the middle row in order to capture extended activity in this region. The $O_{10/05}$ topography, which was irregular, was exhibiting a typical interpolation artifact of the inverse distance weighting scheme, caused by irregular spatial sampling. Indeed, the irregular distances between the optode holders in both the isometric and 10/05 arrangements lead to a nonhomogeneous density of measurement points over the scalp. This artifact did not appear with a DD montage where the sampling points were equidistant to each other. Whereas the $O_{10/05}$ was able to capture the full extent of the GT area, the $R_{10/05}$ maps missed some activity in the center of the GT map, probably because the corresponding SD measurements in the center had a low sensitivity to the targeted VOI.

When adding more than one spatial constraint to the optimization (example in Fig. 7), the double focal VOI and the double symmetrical VOI configurations, O_I and $O_{10/05}$ montages were similarly sensitive to all the target VOIs. On the other hand, the complete montage $R_{10/05}$ was not able to recover activity from the most posterior VOI likely because the VOI was located too deeply in the brain for its sensitivity profile. Such behavior was observed for 2 out of the 20 simulated double VOIs with the $R_{10/05}$ montage.

For the O_I (respectively the $O_{10/05}$), the branch-and-bound algorithm did not allocate positions for optodes over one the VOI for 1 out of 20 simulated double VOIs (respectively 5 out of 20). Such behavior of the algorithm was expected when working with an EEG/fNIRS cap, which features a high density of optode holders, such as the 10/05 cap. In such case, the optimization algorithm may favor one VOI (more likely a superficial one). A weight could be *a priori* attributed to each different VOI in the model to prevent this type of behavior.

Figure 8 displays the distribution of the AUC scores obtained over the 20 simulations and grouped by montage types. For each VOI configuration, the median value for all montages was >0.85, meaning that globally all montages exhibited good detectability performances. As expected, the DD montage showed overall best performance in terms of median and variance of AUC values. For focal VOIs [Fig. 8(a)], the O_I and R_I (respectively, $O_{10/05}$ and $R_{10/05}$) showed very similar performance in terms of median AUC values, suggesting our ability to reach a similar level of detectability with fewer sources and detectors. Results showed slightly more variability for the R_I and $R_{10/05}$ montage than for the O_I and $O_{10/05}$ montage. This interesting property suggests that after optimization of the sensor positions, the topographic maps were less dependent on the location of the VOI. For extended VOIs [Fig. 8(b)], O_I and R_I were showing very similar median AUC values, whereas the median value for the $O_{10/05}$ montage was slightly lower than the median value of the $R_{10/05}$ montage.

In simulations involving more than one VOI [Figs. 8(c) and 8(d)], AUC results obtained with the O_I and the $O_{10/05}$ montages were exhibiting more variability than the regular montages. This was likely due to the fact that fewer sensors were available to accommodate each VOI in configuration involving multiple VOIs. For the $O_{10/05}$ montage, the large variance of AUC values observed in double VOI configurations [Fig. 8(c)] was likely due to the higher proportion of cases in which the branch-and-bound algorithm did not allocate positions for optodes over one VOI as discussed previously.

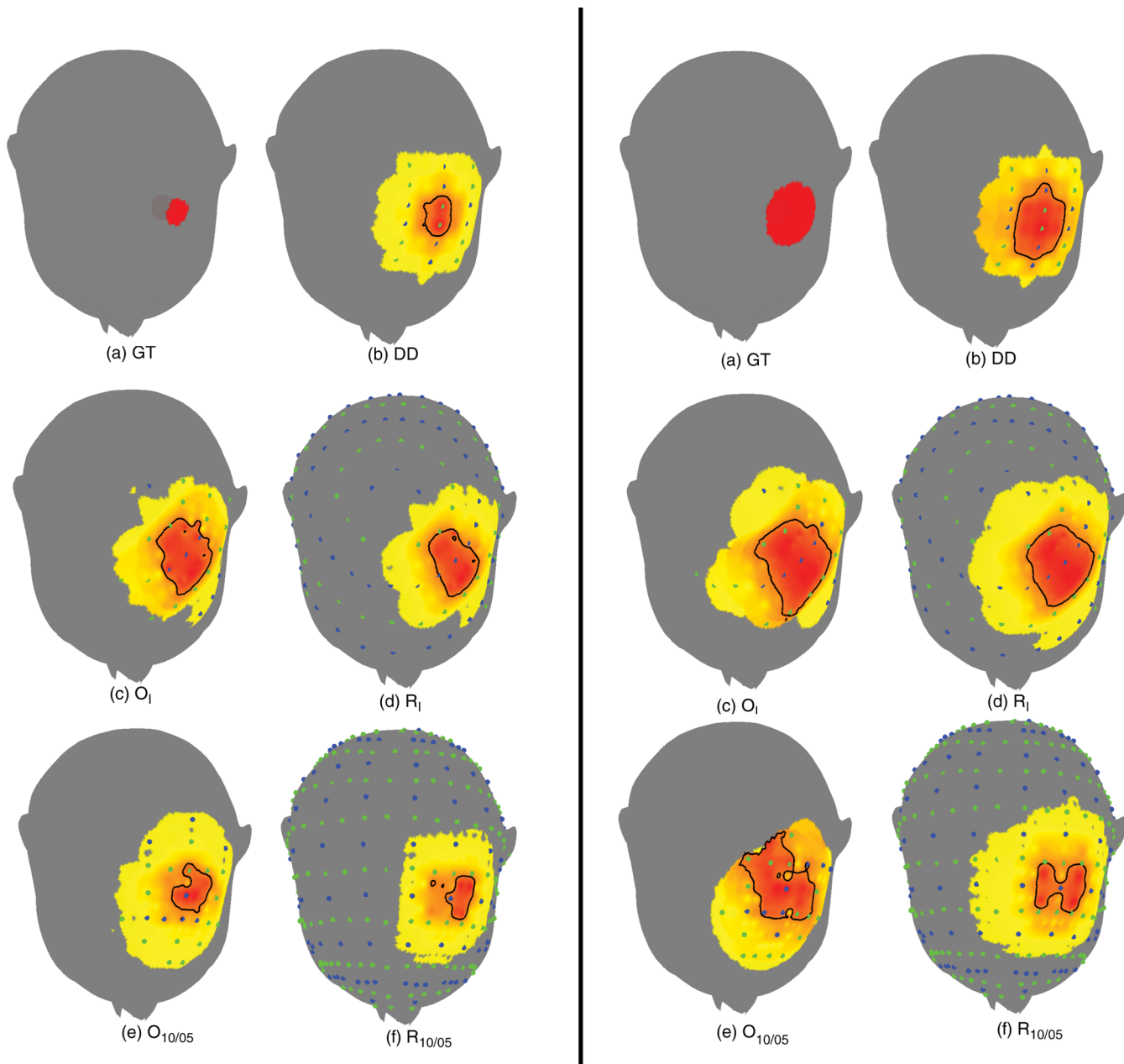


Fig. 6 Amplitude normalized variations of optical densities (ΔOD) topographical maps for one focal (left side) and one extended (right side) VOI configuration. (a) GT, (b) DD, (c) O_I , (d) R_I , (e) $O_{10/05}$, (f) $R_{10/05}$. Sources are in blue and detectors in green.

Figure 9 represents the distribution of the local energy scores defined from the GT area. For all VOI configurations, the O_I montages showed slightly larger LE than the R_I montages and similar variability. On the other hand, the $O_{10/05}$ montages showed clearly larger LE than the $R_{10/05}$ montages and the DD montages in all configurations. These results suggest that we can record localized high amplitude ΔOD measurements over the activation area. The $O_{10/05}$ montage showed the largest LE scores likely due to the fact that it features a denser arrangement of SD pairs, thus allowing more flexibility.

Figure 10 represents the distribution of the ratio of visible voxels and the distribution of the mean overlap score within the visible voxels grouped by montage types. For all VOI

configurations, the optimal montages showed larger ratios of visible voxels than the regular montages suggesting that a larger volume of the target could be detected by optimal montages. For single and double focal VOIs, $\sim 45\%$ of the volume was visible by the optimal and regular montages, whereas for extended VOIs, $\sim 35\%$ of the volume was visible. This decrease was mainly due to the fact that the additional voxels of the extended VOI were localized deeply in the brain and were, therefore, not visible by any SD configuration. The ratio of visible voxels with DD montages was lower for other montages mainly due to its lower density of SD measurements on the scalp. Similar to LE scores, the $O_{10/05}$ montage showed the larger mean overlap value (between 6 and 8), suggesting that the visible voxels are seen by several overlapping SD measurements.

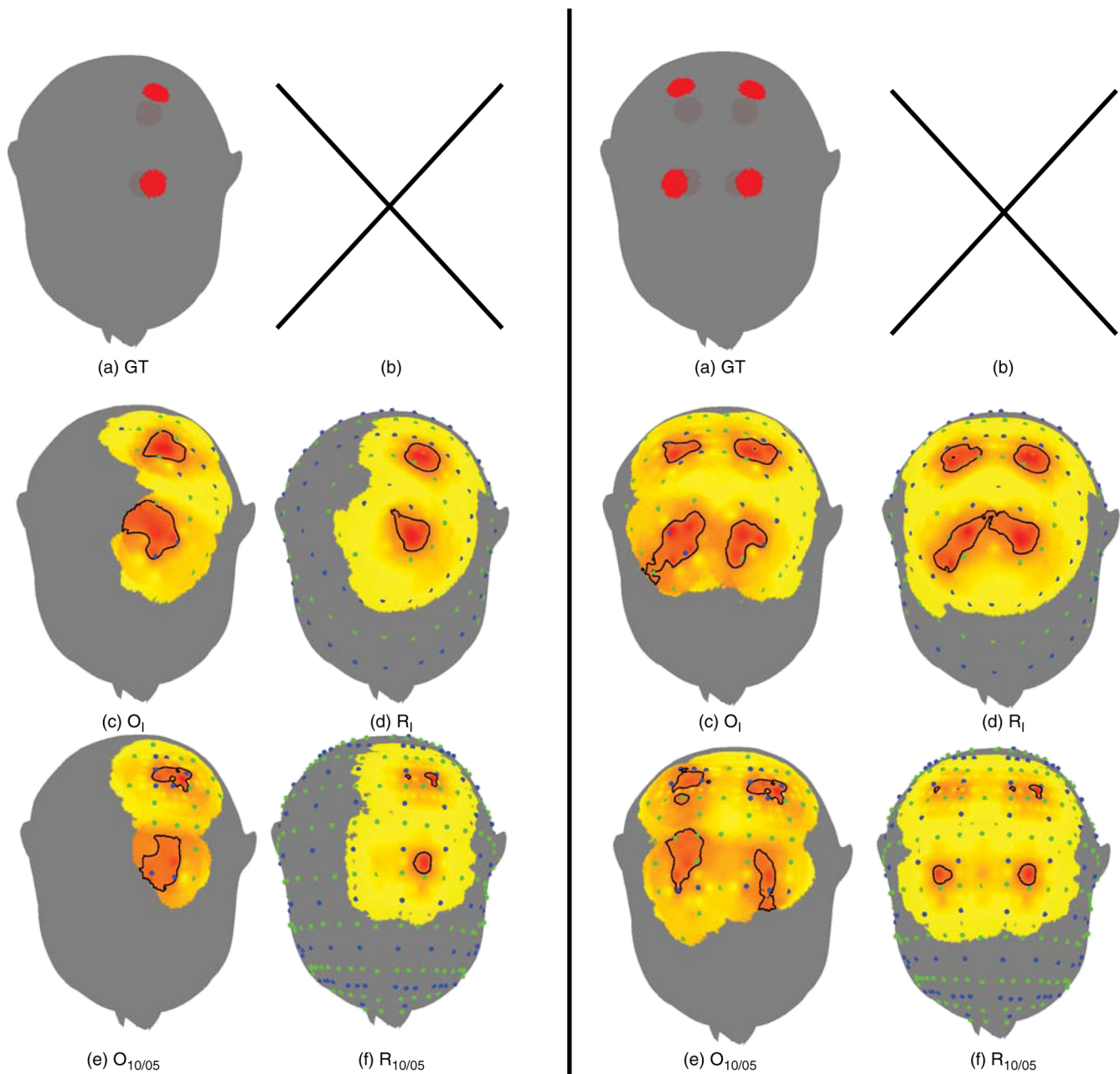


Fig. 7 Amplitude normalized ΔOD topographical maps for one double (left side) and one symmetrical (right side) VOI configuration. (a) GT, (b) the DD montage was not tested in these configurations and replaced by an X, (c) O_1 , (d) R_1 , (e) $O_{10/05}$, (f) $R_{10/05}$. Sources are in blue and detectors in green.

5 Discussion

5.1 Practicability in Epilepsy

Experimentally, even if enough sources and detectors were available from fNIRS system [e.g., the NIRx system (NIRx, USA) allows for 24 dual wavelength sources and 32 detectors], the installation of whole-head montages impose practical challenges. Indeed, the setup times required to attach a large number of optodes on the cap and to check the optical contact quality during the acquisition are limiting factors. In epilepsy, we aim at proposing routinely prolonged EEG/fNIRS recordings (several hours) to increase our chance to record spontaneous epileptic discharges or seizures. Therefore, we need practical and well-

adapted solutions. A first solution would be to choose a subset of these regular whole-head arrangements. However, several challenges would still remain, such as choosing the location of the optode holders to select when targeting several VOIs, coping with the uncertainties of SD sensitivity that depend on the underlying anatomy, and taking into account the variability of the source/detector separation. DD montages cannot be used routinely because they cannot be integrated easily with a clinical arrangement of EEG electrodes.

The proposed method allows the experimenter to choose a limited number of optodes and provides automatically an adequate set of positions for optodes on the EEG/fNIRS cap. The algorithm may be applied easily to any EEG/fNIRS

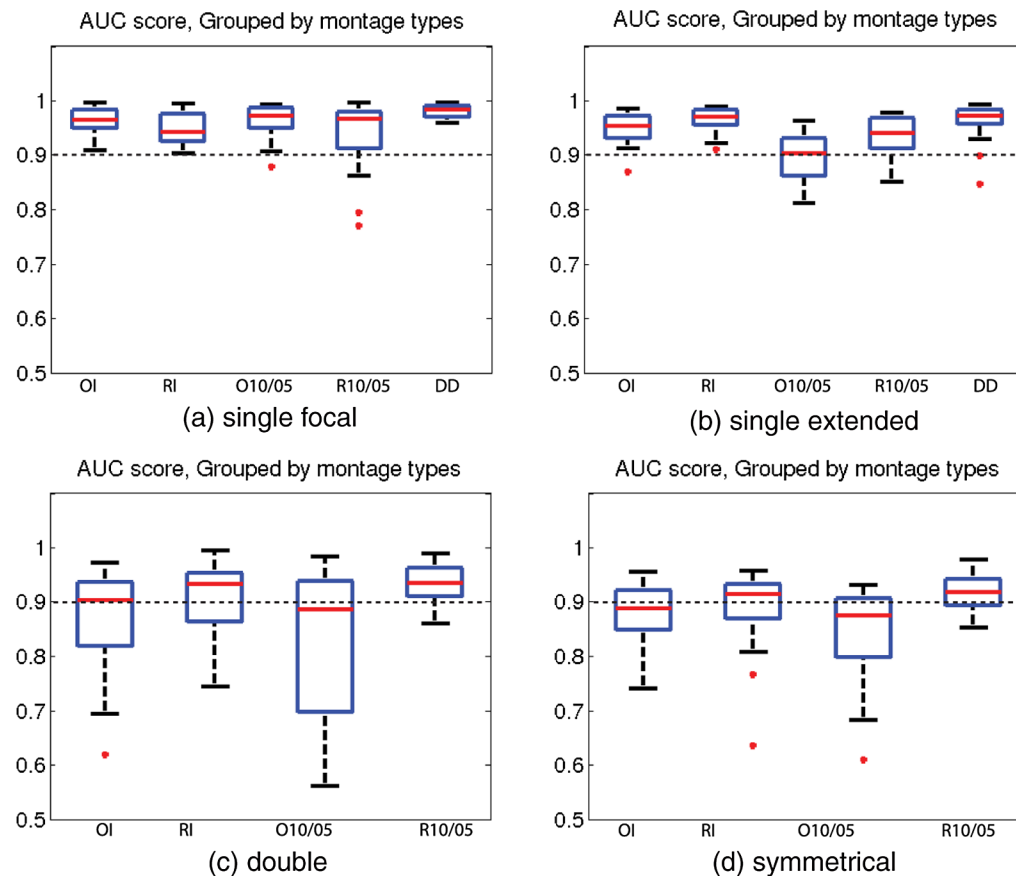


Fig. 8 Area under the receiver operating characteristic curve score distribution grouped by montage types for (a) single focal VOIs, (b) single extended VOIs, (c) double VOIs, (d) symmetrical VOIs.

cap. For instance, the NIRx company (NIRx, USA) proposed a cap that can accommodate up to 256 electrodes or optodes following an extended 10/20 EEG coordinates system.⁶⁹ Ishikawa et al. proposed a whole-head DD configuration⁷⁰ with 128 optode holders and 64 EEG electrode positions interleaved between them.

Our proposed strategy requires some planning. Indeed, the segmentation of the subject anatomical MRI, the digitalization of the EEG/fNIRS cap, the MC simulations, and the montage optimization need to be performed before the acquisition. First, in the context of the presurgical evaluation of patients with epilepsy, collecting and segmenting anatomical MRIs is a typical procedure required by most multimodal imaging investigation (notably EEG/MEG source localization) and would not be specific to EEG/fNIRS. Second, the digitalization of the optode holder positions using theBrainsight neuronavigation system is a fast procedure (<20 min for the isometric EEG/fNIRS cap). Finally, even if modern graphical processing units allow drastic reduction of the computation time, running the MC simulations was the most time-consuming procedure of our proposed method. Because it is not straightforward to predict without prior information on optical sensitivity that a given cortical area is likely to be measurable, we do believe, however, that modeling the light transport in complex head geometries is a necessary step to perform on each specific subject involved in a study in order to get more insights about the origins of the measured fNIRS signal.

In a nonclinical context, when studying a particular brain function among a group of subjects, one can consider using a template MRI and a template of possible fNIRS holders to

design an optimal SD montage for the study. We assume that our approach would still provide relevant information when planning an EEG/fNIRS investigation. Careful evaluation of the added value of our approach when using a template MRI and more simplified model of light transportation would probably be sufficient in such a nonclinical context. We think that our algorithm could accurately provide optimal sets of optode positions in these conditions, but such an evaluation was, however, out of the scope of the present study.

5.2 Optimal Versus Regular Montages

In this study, we compared the montages computed by the optimization algorithm to regular whole-head montages with many sources and detectors (60 sources and 63 detectors for the R_7 montage, 92 sources and 156 detectors for the $R_{10/05}$ montage). Overall, optimal montages showed similar median AUC values and more variability of AUC distributions than our regular montages. However, all AUC values remained within an acceptable range (the median of the distribution was >0.8 for multiple VOIs or 0.9 for single VOIs). For both optimal and whole-head regular montages, the distorted shape of some topographic maps resulted mainly from an interpolation artifact caused by the irregular spatial sampling of measurement points. This problem could be solved using different interpolation schemes. In the case of single VOI configurations (focal or extended), where only a subset of the SD pairs on whole-head montages are sensitive to the target VOI, our results suggest that the optimal montages have resolution characteristics similar to those of

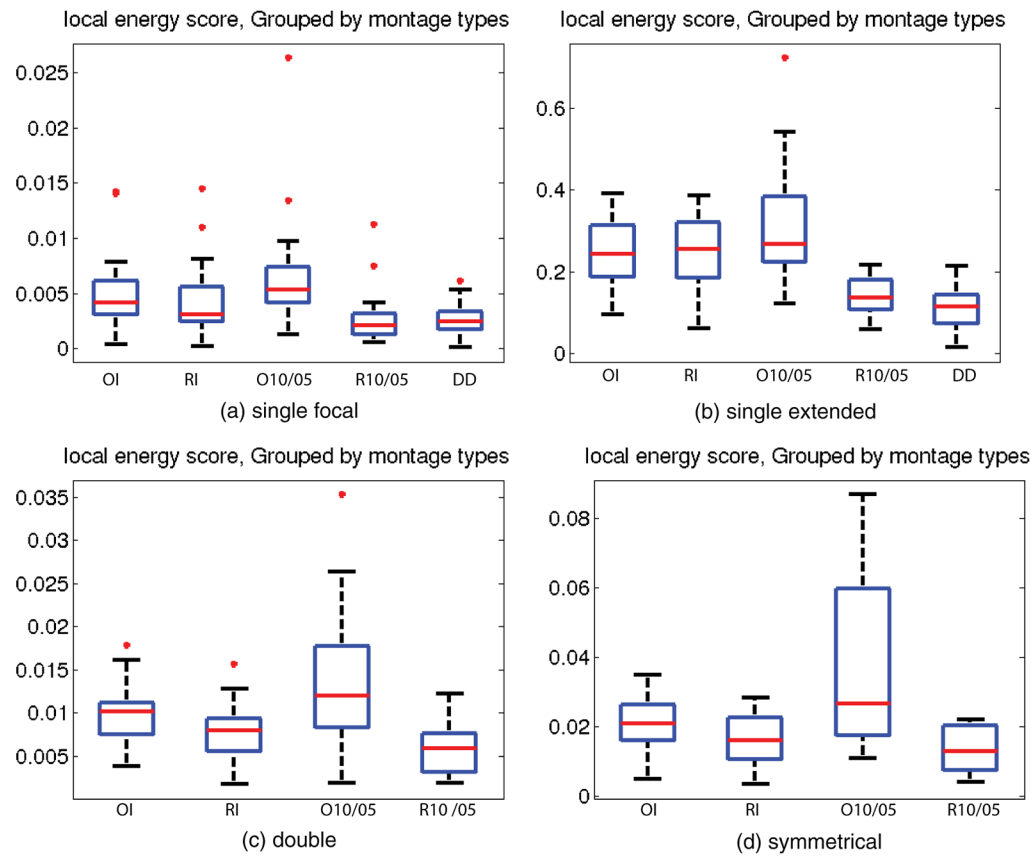


Fig. 9 Local energy score distribution grouped by montage types for (a) single focal VOIs, (b) single extended VOIs, (c) double VOIs, (d) symmetrical VOIs. Note that the graphs are represented with different scales.

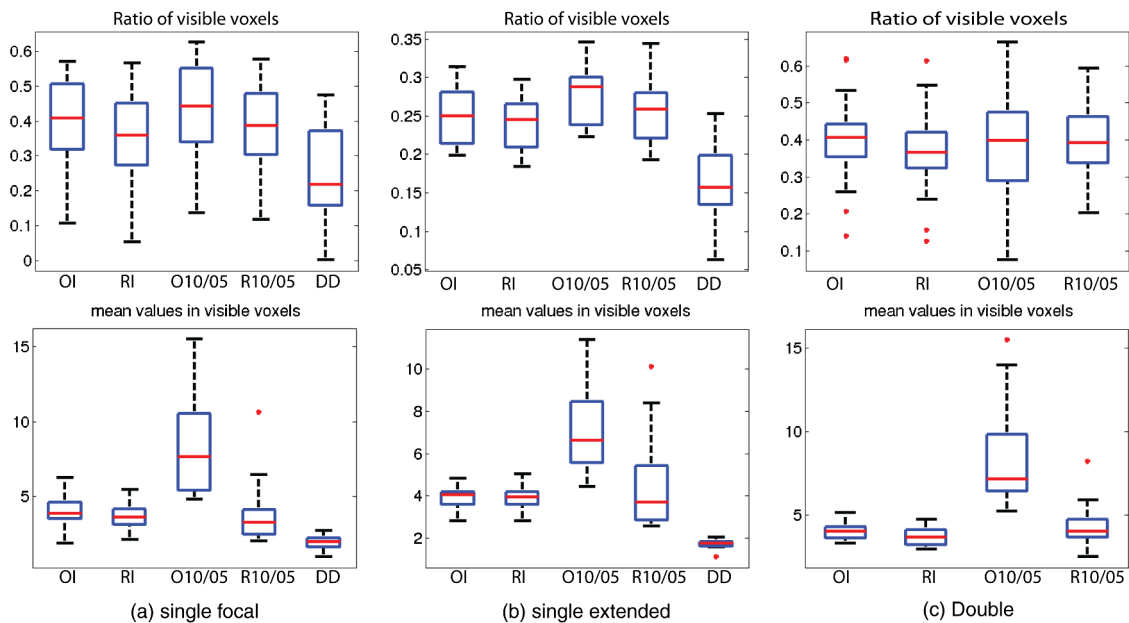


Fig. 10 Ratio of visible voxels (top) and mean overlap score distribution (bottom) grouped by montage types for (a) single focal VOIs, (b) single extended VOIs, (c) double VOIs. Note that the graphs are represented with different scales.

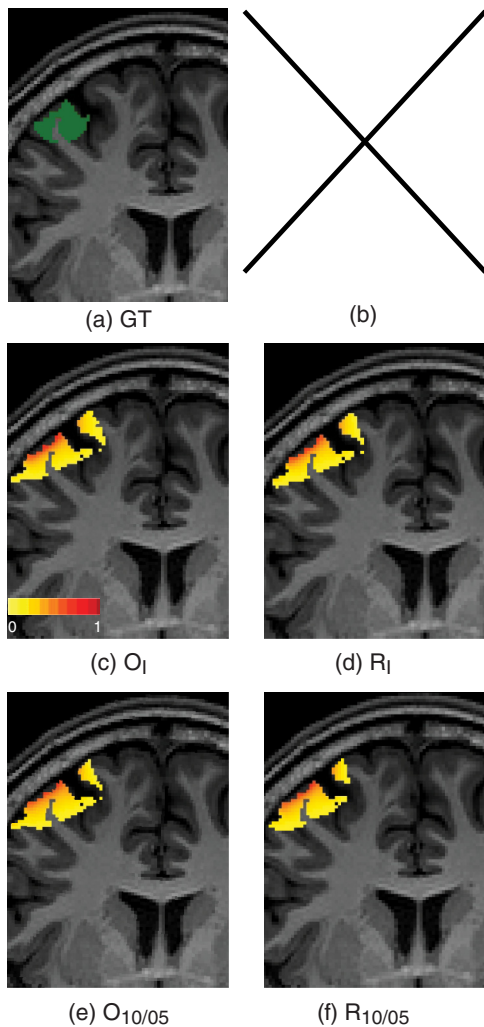


Fig. 11 Representation of the tomographic reconstruction ($\Delta\mu_a^{830}$) of one focal VOI. (a) Simulated VOI, (b) the DD montage was not tested and replaced by an X, (c) O_I , (d) R_I , (e) $O_{10/05}$, (f) $R_{10/05}$ montages.

regular arrangements. In the case of multiple VOIs, we showed that even when using fewer sources and detectors for each target VOI, the estimated optimal montages were able to provide only minimal loss in detectability.

The optimal montages appeared more sensitive than regular montages. First, in some cases, the regular montages were not able to recover the full extent of the GT map (especially the $R_{10/05}$ montage) or were not able to generate topographic maps with equal contrast for multiple VOIs. This was mainly due to the fact that with regular montages the optode positions were not optimized; hence, some SD measurements were not sensitive to the target VOI even when located just above it.

Second, optimal montages showed larger LE values in the GT area than the regular montages. Even the DD montages that have good spatial resolution characteristics were exhibiting lower LE values. These results suggest that high-amplitude OD variations specific to some targeted brain areas are more likely to be captured with optimal montages. Because fNIRS signals are generally contaminated by different systemic physiological interferences coming from the extra cerebral layers,⁷¹ maximizing the sensitivity over cortical areas will tend to improve the SNR of the SD measurements. It means that less physiological interference should be present in the measured signals. Results

in epilepsy mainly reported high SNR hemodynamic responses to seizure or generalized spike and wave,^{30,33,34} but very few studies reported responses to epileptic spikes (brief transient discharge not associated with clinical manifestations).^{31,32} It was demonstrated in these studies that statistical analysis was far from trivial, especially because of the interference from systemic fluctuations. Therefore, improving the SNR seems mandatory for spike analysis and actually we are more concerned about the sensitivity of our measurements than the spatial resolution.

Compared to fMRI, the spatial resolution of fNIRS is limited. fNIRS, however, can provide additional information because of its higher temporal resolution (20 to 100 Hz) and its unique ability to discriminate between $\Delta[\text{HbO}]$ and $\Delta[\text{HbR}]$, which can also provide a measure of the relative change in cerebral blood volume under the assumption of constant hematocrit.⁷² Relative change in cerebral metabolic rate in oxygen and cerebral blood flow may be derived from these quantities in order to investigate possible impairment of neurovascular coupling at the time of epileptic discharges.³⁴

5.3 Perspective

In this study, we did not calculate the $\Delta[\text{HbO}]$ and $\Delta[\text{HbR}]$ topographic maps using the modified Beer–Lambert law mainly because experimentally fNIRS cannot recover accurately $\Delta[\text{HbO}]$ and $\Delta[\text{HbR}]$, especially when dealing with focal activations.⁷³ The MC approach, however, can provide subject-specific estimate of the differential path length and thus improve the quantifications of $\Delta[\text{HbO}]$ and $\Delta[\text{HbR}]$.^{74,75} Note that the unknown partial volume errors⁶² may be estimated *a priori* from the VOI.

It was demonstrated in DOT that high-density montages with overlapping sets of measurements taken near the activated cortical region can greatly improve the spatial resolution and quantitative accuracy of the tomographic images.^{13,20,21,23,24} Interestingly, the optimal montages provide the greatest density of measurement in the targeted VOIs and the highest SNR. Therefore, we may conclude that the optimal montages are well adapted for optical tomography and allow us to solve this ill-posed inverse problem under better conditions. In order to verify this hypothesis, we performed a tomographic reconstruction from the noise-free simulated ΔOD at 830 nm of one focal VOI using the O_I , $O_{10/05}$, R_I , and $R_{10/05}$ montages. To do so, a Tikhonov regularization was used following the approach of White.²⁴ The reconstruction was constrained within the GM. Figure 11 shows the reconstructed $\Delta\mu_a^{830}$ in one coronal slice for the four montages. The original VOI is represented in green in Fig. 11(a). Even if these results are very preliminary, we obtained, with significantly fewer sensors, a DOT accuracy similar to that obtained with the regular montages.

It was demonstrated that the maximum entropy on the mean (MEM) technique is sensitive to the spatial extent of the underlying EEG/MEG sources.⁴⁵ In epilepsy, on the basis of the EEG/fMRI studies, we expect extended hemodynamic activity^{43,47} and we anticipate that the MEM framework will be appropriate for providing DOT reconstructions of epileptic hemodynamic activity. In future studies, we intend to evaluate the performance of MEM in the context of DOT when using optimal montages.

6 Conclusion

In the context of epilepsy research, a specific montage has to be designed specifically for each patient on an EEG/fNIRS cap in

order to visualize image-functional or anatomical regions of interest. Therefore, given a set of available optode holder positions on an EEG/fNIRS cap, we proposed an original method to find the best SD montage automatically. The proposed validation framework included a simulation of focal and extended cortical activity and a comparison of validation metrics across different types of montages. We found that the topographic maps of optimal SD arrangements had spatial resolution properties comparable to those of regular SD arrangements but SNR characteristics that are better than those of SD regular arrangements. Moreover, the optimal montages provided more overlapping measurements, which is an important characteristic when performing DOT.

Acknowledgments

This work was supported by the Natural Sciences and Engineering Research Council of Canada Discovery Grant Program (C.G. and J.M.L.) and a pilot grant from the Quebec Bioimaging Network (QBIN). Electroencephalography/near-infrared spectroscopy equipment was acquired using grants from NSERC Research Tools and Instrumentation Program and the Canadian Foundation for Innovation (C.G.). C.G. and E.K. were also supported by a salary award from the Fonds de Recherche en Santé du Québec (FRQS). A.M. was supported by the Industrial Innovation Scholarships from the Fonds Québécois de la recherche sur la nature et les technologies (FRQNT), NSERC, and the Rogue Research company (Montréal, Canada) joint program. We would like to thank Professor Louis Collins and Dr. Vladimir Fonov for providing us with the the T1 magnetic resonance imaging segmentation and classification method.

References

1. F. Scholkman et al., "A review on continuous wave functional near-infrared spectroscopy and imaging instrumentation and methodology," *NeuroImage* **85**(Part 1), 6–27 (2014).
2. P. W. McCormick et al., "Intracerebral penetration of infrared light. technical note," *J. Neurosurg.* **76**(2), 315–318 (1992).
3. C. Mansouri et al., "Depth sensitivity analysis of functional near-infrared spectroscopy measurement using three-dimensional Monte Carlo modelling-based magnetic resonance imaging," *Lasers Med. Sci.* **25**(3), 431–438 (2010).
4. R. D. Hoge et al., "Investigation of BOLD signal dependence on cerebral blood flow and oxygen consumption: the deoxyhemoglobin dilution model," *Magn. Reson. Med.* **42**(5), 849–863 (1999).
5. D. Boas et al., "Imaging the body with diffuse optical tomography," *IEEE Signal Process. Mag.* **18**(6), 57–75 (2001).
6. H. Koizumi et al., "Optical topography: practical problems and new applications," *Appl. Opt.* **42**(16), 3054–3062 (2003).
7. H. Koizumi et al., "Non-invasive brain-function imaging by optical topography," *Trends Analyt. Chem.* **24**(2), 147–156 (2005).
8. T. Durduran et al., "Diffuse optics for tissue monitoring and tomography," *Rep. Prog. Phys.* **73**(7), 076701 (2010).
9. S. R. Arridge, "Methods in diffuse optical imaging," *Philos. Trans. R. Soc. A* **369**(1955), 4558–4576 (2011).
10. D. T. Delpy et al., "Estimation of optical pathlength through tissue from direct time of flight measurement," *Phys. Med. Biol.* **33**(12), 1433–1442 (1988).
11. L. Kocsis, P. Herman, and A. Eke, "The modified Beer Lambert law revisited," *Phys. Med. Biol.* **51**(5), N91–N98 (2006).
12. H. Kawaguchi, T. Koyama, and E. Okada, "Effect of probe arrangement on reproducibility of images by near-infrared topography evaluated by a virtual head phantom," *Appl. Opt.* **46**(10), 1658–1668 (2007).
13. F. Tian, G. Alexandrakis, and H. Liu, "Optimization of probe geometry for diffuse optical brain imaging based on measurement density and distribution," *Appl. Opt.* **48**(13), 2496–2504 (2009).
14. H. Kakuta and E. Okada, "Evaluation of the position resolution of NIR topography by localised visual stimulation," *Proc. SPIE* **8088**, 80881B (2011).
15. H. Kawaguchi et al., "Theoretical evaluation of accuracy in position and size of brain activity obtained by near-infrared topography," *Phys. Med. Biol.* **49**(12), 2753–2765 (2004).
16. N. Okui et al., "Effect of fibre arrangement on spatial resolution of near-infrared topographic imaging," in *IEEE EMBS Asian-Pacific Conf. on Biomedical Engineering*, Japan, pp. 310–311 (2003).
17. T. Yamamoto et al., "Arranging optical fibres for the spatial resolution improvement of topographical images," *Phys. Med. Biol.* **47**(18), 3429–3440 (2002).
18. T. Yamamoto et al., "Optical fiber arrangement of optical topography for spatial resolution improvement," *Proc. SPIE* **4955**, 487–496 (2003).
19. Y. Yoshida et al., "Phantom experiments for quantitative evaluation of topographic image by mapping algorithm," *Proc. SPIE* **8088**, 80881D (2011).
20. D. A. Boas et al., "Improving the diffuse optical imaging spatial resolution of the cerebral hemodynamic response to brain activation in humans," *Opt. Lett.* **29**(13), 1506–1508 (2004).
21. D. A. Boas, A. M. Dale, and M. A. Franceschini, "Diffuse optical imaging of brain activation: approaches to optimizing image sensitivity, resolution, and accuracy," *NeuroImage* **23**(Suppl 1), S275–S288 (2004).
22. J. P. Culver et al., "Optimization of optode arrangements for diffuse optical tomography: a singular-value analysis," *Opt. Lett.* **26**(10), 701–703 (2001).
23. D. K. Joseph et al., "Diffuse optical tomography system to image brain activation with improved spatial resolution and validation with functional magnetic resonance imaging," *Appl. Opt.* **45**(31), 8142–8151 (2006).
24. B. R. White, "Quantitative evaluation of high-density diffuse optical tomography: in vivo resolution and mapping performance," *J. Biomed. Opt.* **15**(2), 026006 (2010).
25. F. Wallois et al., "Usefulness of simultaneous EEG-NIRS recording in language studies," *Brain Lang.* **121**(2), 110–123 (2012).
26. T. J. Huppert et al., "A temporal comparison of BOLD, ASL, and NIRS hemodynamic responses to motor stimuli in adult humans," *NeuroImage* **29**(2), 368–382 (2006).
27. J. Steinbrink et al., "Illuminating the BOLD signal: combined fMRI fNIRS studies," *Magn. Reson. Imaging* **24**(4), 495–505 (2006).
28. W. Ou et al., "Study of neurovascular coupling in humans via simultaneous magnetoencephalography and diffuse optical imaging acquisition," *NeuroImage* **46**(3), 624–632 (2009).
29. H. Obrig, "NIRS in clinical neurology: a promising tool?," *NeuroImage* **85**(Pt 1), 535–546 (2014).
30. D. K. Nguyen et al., "Non-invasive continuous EEG-fNIRS recording of temporal lobe seizures," *Epilepsy Res.* **99**(1–2), 112–126 (2012).
31. A. Machado et al., "Detection of hemodynamic responses to epileptic activity using simultaneous electro-encephalography (EEG)/near infrared spectroscopy (NIRS) acquisitions," *NeuroImage* **56**(1), 114–125 (2011).
32. P. Pouliot et al., "Nonlinear hemodynamic responses in human epilepsy: a multimodal analysis with fNIRS-EEG and fMRI-EEG," *J. Neurosci. Methods* **204**(2), 326–340 (2012).
33. E. Watanabe et al., "Noninvasive cerebral blood volume measurement during seizures using multichannel near infrared spectroscopic topography," *J. Biomed. Opt.* **5**(3), 287–290 (2000).
34. M. A. Yucel et al., "Reducing motion artifacts for long-term clinical NIRS monitoring using collodion-fixed prism-based optical fibers," *NeuroImage* **85**(Pt 1), 192–201 (2014).
35. G. E. Chatrian, E. Lettich, and P. L. Nelson, "Modified nomenclature for the 10% electrode system," *J. Clin. Neurophysiol.* **5**(2), 183–186 (1988).
36. H. Jasper, "The ten twenty electrode system of the international federation," *Electroencephalogr. Clin. Neurophysiol.* **10**, 371–375 (1958).
37. P. Giacometti and S. G. Diamond, "Compliant head probe for positioning electroencephalography electrodes and near-infrared spectroscopy optodes," *J. Biomed. Opt.* **18**(2), 027005 (2013).
38. V. Jurcak, D. Tsuzuki, and I. Dan, "10/20, 10/10, and 10/5 systems revisited: their validity as relative head-surface-based positioning systems," *NeuroImage* **34**(4), 1600–1611 (2007).
39. K. L. Perdue, Q. Fang, and S. G. Diamond, "Quantitative assessment of diffuse optical tomography sensitivity to the cerebral cortex using a whole-head probe," *Phys. Med. Biol.* **57**(10), 2857–2872 (2012).

40. F. Pittau, F. Dubeau, and J. Gotman, "Contribution of EEG/fMRI to the definition of the epileptic focus," *Neurology* **78**(19), 1479–1487 (2012).
41. O. Colliot et al., "Segmentation of focal cortical dysplasia lesions on MRI using level set evolution," *NeuroImage* **32**(4), 1621–1630 (2006).
42. V. Brodbeck et al., "Electroencephalographic source imaging: a prospective study of 152 operated epileptic patients," *Brain* **134**(Pt 10), 2887–2897 (2011).
43. C. Grova et al., "Concordance between distributed EEG source localization and simultaneous EEG-fMRI studies of epileptic spikes," *NeuroImage* **39**(2), 755–774 (2008).
44. Z. Agirre-Arrizubieta et al., "Interictal magnetoencephalography and the irritative zone in the electrocorticogram," *Brain* **132**(Pt 11), 3060–3071 (2009).
45. R. A. Chowdhury et al., "MEG source localization of spatially extended generators of epileptic activity: comparing entropic and hierarchical Bayesian approaches," *PLoS ONE* **8**(2), e55969 (2013).
46. J. Gotman et al., "Combining EEG and fMRI: a multimodal tool for epilepsy research," *J. Magn. Reson. Imaging* **23**(6), 906–920 (2006).
47. S. Vulliemoz et al., "The combination of EEG source imaging and EEG-correlated functional MRI to map epileptic networks," *Epilepsia* **51**(4), 491–505 (2010).
48. S. S. Spencer, "Neural networks in human epilepsy: evidence of and implications for treatment," *Epilepsia* **43**(3), 219–227 (2002).
49. A. Land and A. Doig, "An automatic method of solving discrete programming problems," *Econometrica* **28**, 497–520 (1960).
50. R. Oostenveld and P. Praamstra, "The five percent electrode system for high-resolution EEG and ERP measurements," *Clin. Neurophysiol.* **112**(4), 713–719 (2001).
51. S. R. Arridge, "Optical tomography in medical imaging," *Inverse Probl.* **15**, R41–R93 (1999).
52. D. Boas et al., "Three dimensional Monte Carlo code for photon migration through complex heterogeneous media including the adult human head," *Opt. Express* **10**(3), 159–170 (2002).
53. F. B. Haeussinger et al., "Simulation of near-infrared light absorption considering individual head and prefrontal cortex anatomy: implications for optical neuroimaging," *PLoS ONE* **6**(10), e26377 (2011).
54. E. Okada, "The effect of superficial tissue of the head on spatial sensitivity profiles for near infrared spectroscopy and imaging," *Opt. Rev.* **7**(5), 375–382 (2000).
55. Q. Fang and D. A. Boas, "Monte Carlo simulation of photon migration in 3D turbid media accelerated by graphics processing units," *Opt. Express* **17**(22), 20178–20190 (2009).
56. L. A. Wolsey and G. L. Nemhauser, *Integer and Combinatorial Optimization*, Wiley, Hoboken, NJ (1999).
57. V. Chvatal, *Linear Programming*, W. H. Freeman, New York, NY (1983).
58. D. L. Collins et al., "Automatic 3D model based neuroanatomical segmentation," *Hum. Brain Mapp.* **3**(3), 190–208 (1995).
59. P. Coupe et al., "Patch-based segmentation using expert priors: application to hippocampus and ventricle segmentation," *NeuroImage* **54**(2), 940–954 (2011).
60. V. Fonov et al., "Unbiased average age-appropriate atlases for pediatric studies," *NeuroImage* **54**(1), 313–327 (2011).
61. B. Aubert-Broche, A. C. Evans, and L. Collins, "A new improved version of the realistic digital brain phantom," *NeuroImage* **32**(1), 138–145 (2006).
62. G. Strangman, M. A. Franceschini, and D. A. Boas, "Factors affecting the accuracy of near-infrared spectroscopy concentration calculations for focal changes in oxygenation parameters," *NeuroImage* **18**(4), 865–879 (2003).
63. B. K. P. Horn, "Closed-form solution of absolute orientation using unit quaternions," *J. Opt. Soc. Am. A* **4**(4), 629–642 (1987).
64. F. Tadel et al., "Brainstorm: a user-friendly application for MEG/EEG analysis," *Comput. Intell. Neurosci.* **2011**, 879716 (2011).
65. T. Aihara et al., "Cortical current source estimation from electroencephalography in combination with near-infrared spectroscopy as a hierarchical prior," *NeuroImage* **59**(4), 4006–4021 (2012).
66. M. Takeuchi et al., "Brain cortical mapping by simultaneous recording of functional near infrared spectroscopy and electroencephalograms from the whole brain during right median nerve stimulation," *Brain Topogr.* **22**(3), 197–214 (2009).
67. C. E. Metz, "ROC methodology in radiologic imaging," *Invest. Radiol.* **21**(9), 720–733 (1986).
68. C. Grova et al., "Evaluation of EEG localization methods using realistic simulations of interictal spikes," *NeuroImage* **29**(3), 734–753 (2006).
69. S. Fazli et al., "Enhanced performance by a hybrid NIRS-EEG brain computer interface," *NeuroImage* **59**(1), 519–529 (2012).
70. A. Ishikawa et al., "Development of double density whole brain fNIRS with EEG system for brain machine interface," in *Annual Int. Conf. of the IEEE Engineering in Medicine and Biology Society*, Boston, pp. 6118–6122, IEEE Engineering in Medicine and Biology Society (2011).
71. E. Kirilina et al., "The physiological origin of task-evoked systemic artefacts in functional near infrared spectroscopy," *NeuroImage* **61**(1), 70–81 (2012).
72. A. M. Siegel et al., "Temporal comparison of functional brain imaging with diffuse optical tomography and fMRI during rat forepaw stimulation," *Phys. Med. Biol.* **48**(10), 1391–1403 (2003).
73. D. A. Boas et al., "The accuracy of near infrared spectroscopy and imaging during focal changes in cerebral hemodynamics," *NeuroImage* **13**(1), 76–90 (2001).
74. C. Bonnerly et al., "Changes in diffusion path length with old age in diffuse optical tomography," *J. Biomed. Opt.* **17**(5), 056002 (2012).
75. T. Talukdar, J. H. Moore, and S. G. Diamond, "Continuous correction of differential path length factor in near-infrared spectroscopy," *J. Biomed. Opt.* **18**(5), 056001 (2013).

Alexis Machado is a PhD student in the McGill University Department of Biomedical Engineering. He obtained a master's degree in biomedical engineering from the École Polytechnique de Montréal, Canada. His research interests are in statistical signal processing and localization of epileptic spikes using diffuse optical imaging.

Odile Marcotte is an adjunct professor in the Department of Computer Science of the Université du Québec à Montréal and deputy director of the Centre de recherches mathématiques (Université de Montréal). She obtained a master's degree in operations research from the École Polytechnique de Montréal and a PhD in operations research from Cornell University. Her research interests are in graph theory, combinatorial optimization, and integer programming.

Jean Marc Lina received an electrical engineering diploma from the National Polytechnic Institute of Grenoble, France, in 1982 and a PhD in theoretical physics from the Université de Montréal, Canada, in 1990. He is currently a professor in the electrical engineering department of the École de Technologie Supérieure and a member of the Centre de Recherches Mathématiques, Université de Montréal. His current research interests include wavelet analyses, inverse problems, entropic inference, and probabilistic graphical models applied to electromagnetic neuroimaging.

Eliane Kobayashi obtained her medical degree at UNICAMP, Brazil, where she also completed the neurology residency program, the epilepsy fellowship, and PhD studies. She came to the Montréal Neurological Institute (MNI) for postdoctoral studies. She is an assistant professor in the Department of Neurology and Neurosurgery at McGill University. She works as an epileptologist and neurophysiologist at the MNI Epilepsy Service and EEG Department. She received the Early Career Physician Scientist Award from the American Epilepsy Society.

Christophe Grova received an engineering and a MSc degrees in biomedical engineering (University of Technology of Compiègne, France), followed by a PhD in medical imaging (University of Rennes, France). Then, he came at the MNI as a postdoctoral fellow. Since 2008, he is assistant professor in Biomedical Engineering and Neurology and Neurosurgery Departments (McGill University). His research aims at investigating the integration of multimodal functional data to study brain mechanisms during epileptic discharges.